Available online at www.sciencedirect.com
ScienceDirect
Nuclear Instruments and Methods in Physics Research A 568 (2006) 488–502
NUCLEAR INSTRUMENTS & METHODS IN PHYSICS RESEARCH Section A
www.elsevier.com/locate/nima

RF deflector design and measurements for the longitudinal and transverse phase space characterization at SPARC

David Alesini[a,*], Giampiero Di Pirro[a], Luca Ficcadenti[b], Andrea Mostacci[b], Luigi Palumbo[b], James Rosenzweig[c], Cristina Vaccarezza[a]

[a]*INFN-LNF, Via E. Fermi 40, I-00044 Frascati, Italy*
[b]*Università degli Studi di Roma La Sapienza, Dip. Energetica, Via A. Scarpa 14, 00161, Roma, Italy*
[c]*Department of Physics and Astronomy, UCLA, 405 Hilgard Avenue, Los Angeles, CA 90095, USA*

Received 10 July 2006; received in revised form 12 July 2006; accepted 15 July 2006
Available online 22 August 2006

Abstract

The six-dimensional beam phase space at the exit of a photoinjector can be completely characterized by means of an RF deflector and a dispersive system. In this paper we summarize the main features of the use of an RF deflector to measure aspects of the longitudinal and transverse phase space in an ultra-short electron beam. In particular we illustrate these measurements through the simulation of experiments currently under development at the SPARC photoinjector. We also discuss the design procedure followed to design the RF deflector for SPARC. This device is a five-cell structure operating on the π mode at 2.856 GHz. Finally, we report and discuss the cold-test measurement results on a full scale aluminum prototype.

PACS: 41.75−i; 41.60.Cr; 41.85.Ew

Keywords: High-brightness beam diagnostics; RF design and measurements; Soft X-ray FEL

1. Introduction

The main goals of the SPARC [1] injector project are the (1) generation of a high brightness electron beam able to drive a self-amplified spontaneous free-electron laser (SASE-FEL) experiment in the green visible light and (2) the development of an ultra-brilliant beam photoinjector needed for the future SASE-FEL-based X-ray sources.

The characterization of the longitudinal and transverse phase space of the beam at the injector exit is crucial, as it allows the tuning and verification of all the photoinjector performance parameters. These parameters concern physical phenomena which occur on a time scale much shorter than a picosecond, thus making time-resolved measurements extremely challenging. With the use of an RF deflector it is possible to measure the bunch length [2,3] at this level, however. The addition of a dispersive system further allows the measurement of the longitudinal beam phase space distribution. Similarly, since the longitudinal beam distribution can be projected along a transverse coordinate, the transverse emittance of each longitudinal bunch slice can be measured using the quadrupole scan technique [4–6].

In the second section of this paper we briefly review the basic principles of the longitudinal and transverse beam phase space characterization using an RF deflector. In the third section we show the simulation of the measurements in the case of the SPARC photoinjector. In particular we illustrate the longitudinal phase space measurement (Section 3.1) and the horizontal beam slice emittance measurement (Section 3.2). In the fourth section we illustrate the procedure followed to design the RF deflector for SPARC (Sections 4.1 and 4.2) and the RF measurement results on a full scale aluminum prototype (Section 5). Finally, in the last section, we briefly illustrate the RF deflector power feeding system that we are planning to use.

*Corresponding author. Tel.: +39 06 94032639; fax: +39 06 94032256.
E-mail address: alesini@lnf.infn.it (D. Alesini).

0168-9002/$ - see front matter © 2006 Elsevier B.V. All rights reserved.
doi:10.1016/j.nima.2006.07.050

2. Longitudinal and transverse beam phase space characterization using an RF deflector

The effect of the RF deflector on a beam traveling along the z direction is sketched in Fig. 1: the RF deflector voltage (the integrated transverse Lorenz force per unit charge) is null in the center of the bunch and gives a linear transverse deflection to the head and tail of bunch. After the deflector, at the position of the flag, the transverse kick (vertical, for example) results in a transverse displacement of the centroid of each bunch slice proportional to the slice longitudinal position with respect to the bunch center. If the bunch length is L_B, the vertical dimension of the bunch at the flag, neglecting the vertical beam emittance of the bunch, is given by:

$$y_B = \sqrt{\beta_{y\_\mathrm{defl}}\beta_{y\_\mathrm{flag}}}\sin(\Delta\Phi)\frac{V_\mathrm{T}}{(E/e)}\sin\left(\omega_\mathrm{RF}L_B/2c\right) \underbrace{\cong}_{\lambda_\mathrm{RF}\gg L_B} \frac{\omega_\mathrm{RF}L_B V_\mathrm{T}\sqrt{\beta_{y\_\mathrm{defl}}\beta_{y\_\mathrm{flag}}}\sin(\Delta\Phi)}{2cE/e} \quad (1)$$

where β_{y_defl} and β_{y_flag} are the vertical β functions at the deflector and flag position, respectively, $\Delta\Phi$ is the phase advance between the deflector and the flag, ω_RF the angular frequency of the deflecting voltage, V_T the peak transverse voltage, and E the beam energy in eV units. If we consider a simple drift space of length L between the deflector and the flag, the Eq. (1) reduces to:

$$y_B = \frac{\omega_\mathrm{RF}LL_B V_\mathrm{T}}{2cE/e}. \quad (2)$$

Eqs. (1) and (2) show that the longitudinal bunch distribution can be measured by measuring the transverse bunch distribution after the deflector.

In the actual case, the transverse distribution of the bunch at the flag position is the superposition between the deflected beam size and the vertical dimension of the bunch slices at the flag position (σ_y), as illustrated in Fig. 1. The rms resolution length (L_res) can be defined as the bunch length that gives, on the flag, a vertical spot exactly equal to σ_y. From the previous expressions it is easy to verify that:

$$L_\mathrm{res} \cong \frac{cE/e\sqrt{\varepsilon_y}}{\omega_\mathrm{RF}\sqrt{\beta_{y\_\mathrm{defl}}}\sin(\Delta\Phi)V_\mathrm{T}} \quad (3)$$

where ε_y is the transverse vertical emittance of the beam. In the case of a drift space this expression becomes:

$$L_\mathrm{res} = \frac{\sigma_y cE/e}{\omega_\mathrm{RF}LV_\mathrm{T}} = \frac{cE/e\sqrt{\varepsilon_y\beta_{y\_\mathrm{flag}}}}{\omega_\mathrm{RF}LV_\mathrm{T}} \quad (4)$$

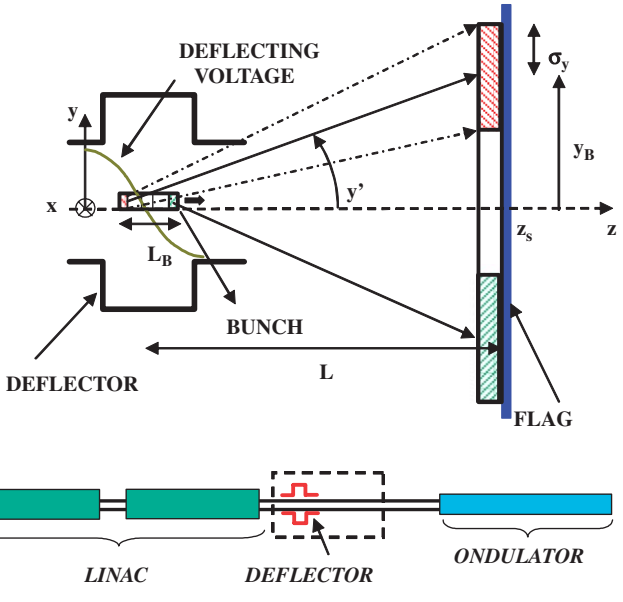

Fig. 1. Bunch length measurement schematic setup using an RF deflector.

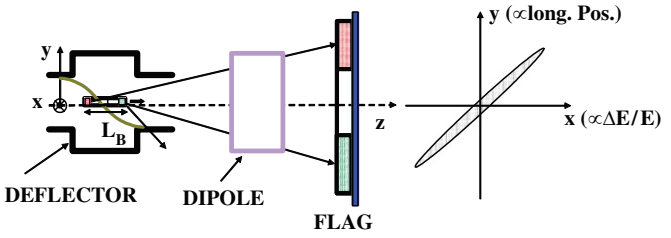

Fig. 2. Longitudinal phase space measurement setup using an RF deflector and a dipole magnet.

A sketch of the complete longitudinal phase space measurement setup is shown in Fig. 2. In this scenario, the bunch is vertically deflected by the RF deflector and horizontally by a magnetic dipole. The dispersion properties of the dipole allow to completely characterize the energy distribution of each bunch slice reconstructing the longitudinal phase space. In this case the rms energy spread resolution is simply given by:

$$\left.\frac{\Delta E}{E}\right|_\mathrm{res} = \frac{\sqrt{\varepsilon_x\beta_{x\_\mathrm{flag}}}}{D_\mathrm{flag}} \quad (5)$$

where ε_x, β_{x_flag} and D_flag are the horizontal emittance, the horizontal β function and dispersion at the flag position, respectively.

With the deflector it is also possible to measure the horizontal beam slice emittance: the deflecting voltage gives the correlation between the longitudinal slice position and the vertical coordinate and the horizontal emittance can be measured with the quadrupole scan technique. This scheme is conceptually illustrated in Fig. 3.

3. Simulation of the measurements for SPARC

The SPARC photoinjector layout, given in Fig. 4, consists of:

(a) 1.6-cell RF gun of the BNL/UCLA/SLAC type [7] operating at S band (2856 MHz) with incorporated metallic photocathode (Cu or Mg) and generating a 6 MeV electron beam;

(b) two accelerating sections of the SLAC type (S band, traveling wave).

The beam parameter list at the end of the injector is reported in Table 1.

A detailed layout of the magnets and measurement flags that will be used for the longitudinal and transverse phase space characterization is reported in Fig. 5.

The longitudinal beam profile will be measured using the RF deflectors and directly analyzing the image produced by the beam on the flag F0 while the complete longitudinal phase space will be reconstructed using the RF deflector in combination with the dipole magnet and analyzing the image produced by the beam on the flag F1.

Using the RF deflector the horizontal slice emittance can be measured either on the transfer lines or on the dogleg, at the flags F0 or F3, respectively.The first two quadrupoles after the linac sections, Q_T1 and Q_T2, are used, in this case, for the quadrupole scan.

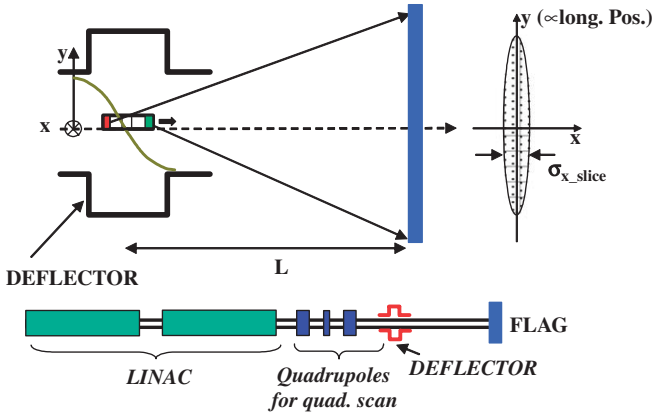

Fig. 3. Horizontal slice emittance measurement schematic setup using an RF deflector.

3.1. Simulation of the longitudinal phase space measurement

In the SPARC case, using Eq. (4) it is possible to calculate the longitudinal resolution L_{res} as a function of the deflecting voltage V_T. The result is plotted in Fig. 6 assuming $L = 2$ m and $\sigma_y = 30$ μm at the flag position. In the SPARC case since the rms bunch length is about 1 mm, an rms resolution length of the order of 100 μm is sufficient. Therefore a deflecting voltage of 1 MV can be chosen as the required RF deflector voltage for SPARC.

A beam represented by 1.5×10^5 particles obtained from PARMELA [8] simulation at the end of the SPARC LINAC section has been tracked with the ELEGANT [9] code along the SPARC transfer lines. The beam images obtained at the RF deflector location and at the flag location, F0, are shown in Fig. 7.

The results of the data analysis are shown in Fig. 8 where the vertical profile of the beam at the flag with $V_T = 1$ MV and the longitudinal distribution of the bunch are displayed. The value of σ_z as obtained by applying

Table 1
Beam parameter list at the end of the SPARC injector

Electron beam energy (MeV)	155
Bunch charge (nC)	1.1
Repetition rate (Hz)	10
Cathode peak field (MV/m)	120
Photocathode spot size (mm)	1.13
Laser pulse duration (ps)	10
Bunch energy at gun exit (MeV)	5.6
Bunch peak current at linac exit (A)	100
RMS normalized transverse emittance at linac exit (mm mrad)	<2
RMS slice normalized transverse emittance at linac exit (300 μm slice) (mm mrad)	<1
RMS longitudinal emittance at linac exit (deg keV)	1000
RMS energy spread (%)	0.2
RMS bunch length at LINAC exit (mm)	1

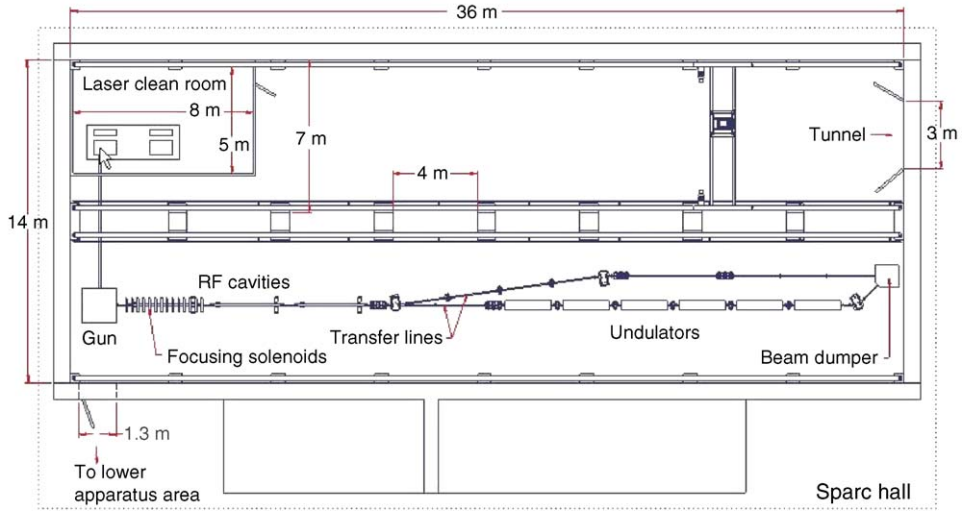

Fig. 4. SPARC photoinjector layout.

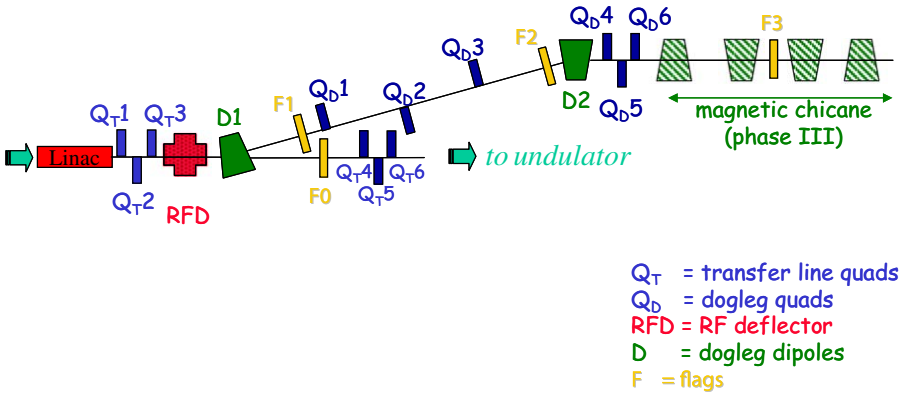

Fig. 5. Schematic layout of the magnets at the end of the SPARC photoinjector for longitudinal and transverse phase space characterization with an RF deflector.

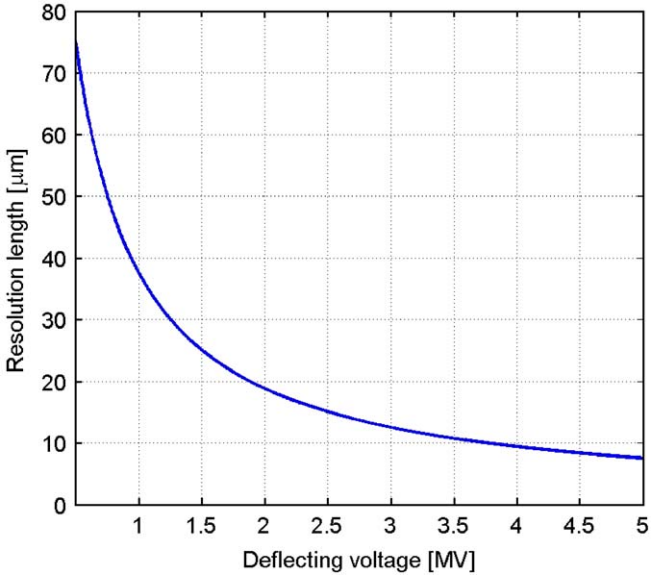

Fig. 6. Resolution length as a function of the deflecting voltage.

Eq. (2) and by the longitudinal analysis of the raw data obtained from ELEGANT tracking agree with an error smaller than 1%.

The images collected on the dogleg at the flag located in F1 show the complete reconstruction of the longitudinal phase space as shown in Fig. 9, where the time–energy (t,p) distribution is replicated in the transverse plane (y,x). The "reconstructed" longitudinal phase space is in very good agreement with the real one.

3.2. Transverse phase space

The measurement of the beam slice emittance in the horizontal plane can be done with the quadrupole scan looking at the beam size at the flag locations F0 or F3, where two different values of image resolution can be achieved for the minimum horizontal rms size reconstruction. The optical functions of the SPARC transfer lines and dogleg for the measurement setup of the horizontal emittance are shown in Fig. 10.

In Fig. 11 the beam horizontal slice emittance is given together with the two simulated measurements at F0 (b) and F3 (c), respectively. Between the two flags it is possible to achieve two different resolutions, investigating a wide range of beam emittance values [10].

4. RF deflector design

The required transverse deflecting voltage $V_T = 1\,\mathrm{MV}$ can be, in principle, achieved by both traveling wave (TW) or standing wave (SW) structures. In our case the choice between the two solutions is related to the maximum available input power (2 MW as shown in paragraph 5), space (about 0.4 m) and RF pulse length ($\approx 5\,\mu\mathrm{s}$). Scaling known deflecting TW structures [11] to the SPARC frequency ($f_{RF} = 2.856\,\mathrm{GHz}$) it follows that, to achieve the required deflecting voltage, the length of the deflector has to be $\approx 0.4\,\mathrm{m}$ with a total number of cells equal to about 12. As shown in detail in the next paragraphs the same voltage can be achieved with a single SW cavity of about 0.05 m long. To allow reaching better resolution and flexibility, also considering longitudinal compression experiments in the next phases of SPARC [1], it has been proposed to adopt a 5-cell SW structure operating on the π mode. As shown in the next paragraphs, this structure allows reaching a maximum transverse deflecting voltage of more than 3 MV with low peak surface electric field. Moreover the power to feed the cavity can be split from the SPARC RF gun klystron waveguide by a 10 dB directional coupler (see Section 6). Adopting this solution, the circulator and the directional coupler itself preserve the klystron and the RF gun from the cavity reflected power. We will first address the two dimensional design of the structure (Section 4.1), i.e., without including the coupler and tuning system which are separately discussed later (Section 4.2).

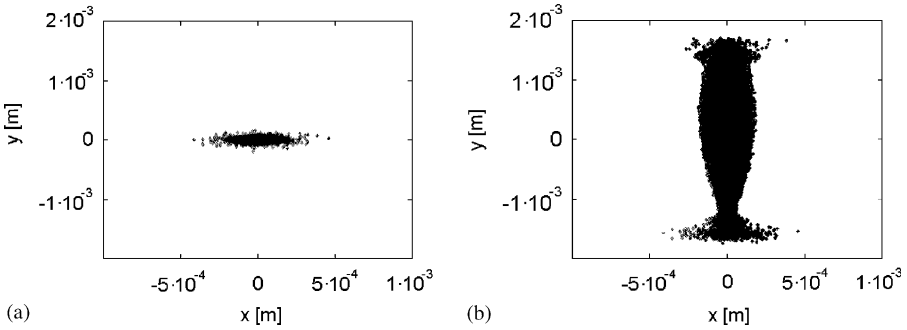

Fig. 7. (a) Bunch transverse distribution at the RF deflector location and (b) bunch transverse distribution at the flag location.

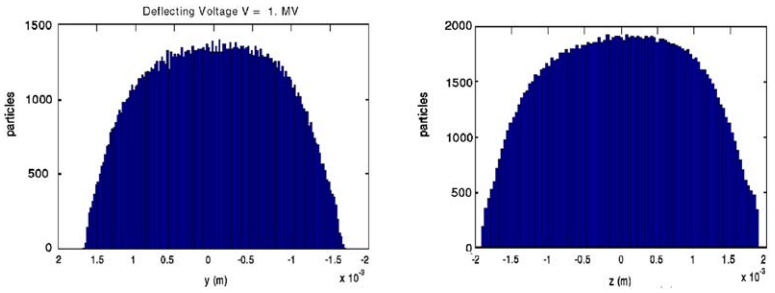

Fig. 8. Above: the longitudinal bunch distribution as projected by the RF deflector on the vertical coordinate of the flag F0; below: the same bunch longitudinal distribution vs. longitudinal coordinates (z-axis).

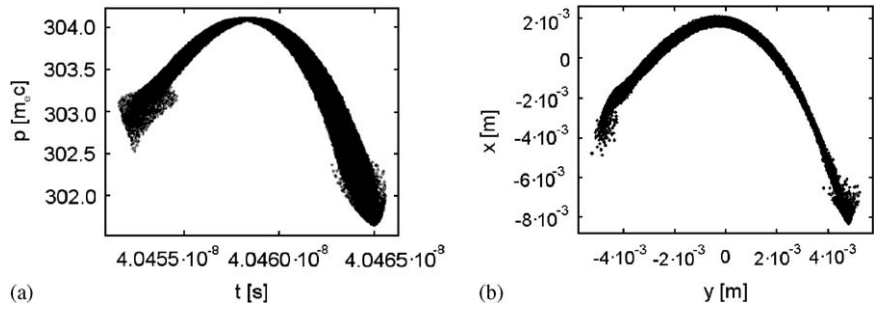

Fig. 9. (a) Bunch longitudinal phase space at F1 and (b) bunch transverse distribution at F1 after deflection.

4.1. Two-dimensioal design and electromagnetic characterization

To illustrate the procedure followed to design the 5-cell RF deflector, let us start with the single-cell design. The first deflecting mode in a pillbox cavity is the TM_{110} mode and the deflection is given by the B field [12] only. In a single cell with irises (sketched in Fig. 12) there is a transverse E-field component that contributes to the total deflection (see Fig. 13). The ratio between the electric and the magnetic deflection contributions is strongly dependent on the iris aperture and can be from 10% for small irises to 90% for large irises apertures.

To adapt the cell design to the SPARC requirements, the inner radius a has been chosen equal to the SPARC beam pipe radius (20 mm), the cell length d equal to $c/2f_{RF}$ (with c speed of light) to synchronize the bunch passage and the π-mode deflecting field while the external radius b has been tuned to set up the resonant frequency[1] at 2.856 GHz by using the electromagnetic (EM) codes MAFIA [13] and HFSS [14]. The iris thickness t has been chosen at a reasonable value of 9.5 mm, considering that it is not a critical dimension in term of power dissipation, frequency sensitivities and deflection efficiency. The single-cell final dimensions, parameters and frequency sensitivities, are reported in Table 2 assuming copper material. We have defined the transverse shunt impedance by the formula:

$$R_T = \frac{\left|\int_0^{L_c} (cB_x + E_y) e^{j\omega_{RF} z/c}\, dz\right|^2}{2P} \quad (6)$$

[1]In the single-cell simulations perfect magnetic boundary conditions on the iris planes have been assumed.

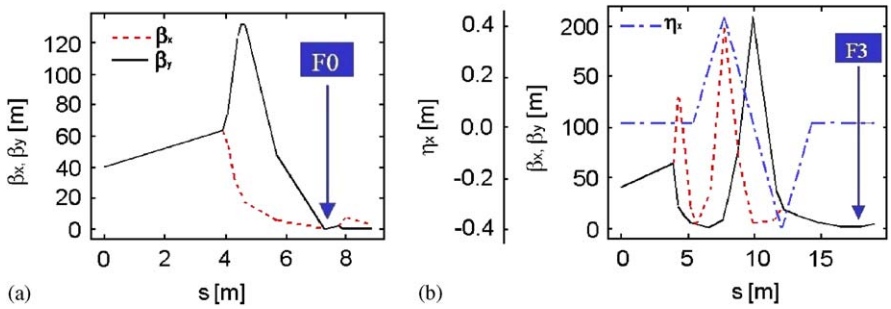

Fig. 10. SPARC transfer line optic functions for the horizontal quadrupole scan at F0 (left) and F3 (right). The origin of the longitudinal coordinate corresponds to the exit of the second linac section.

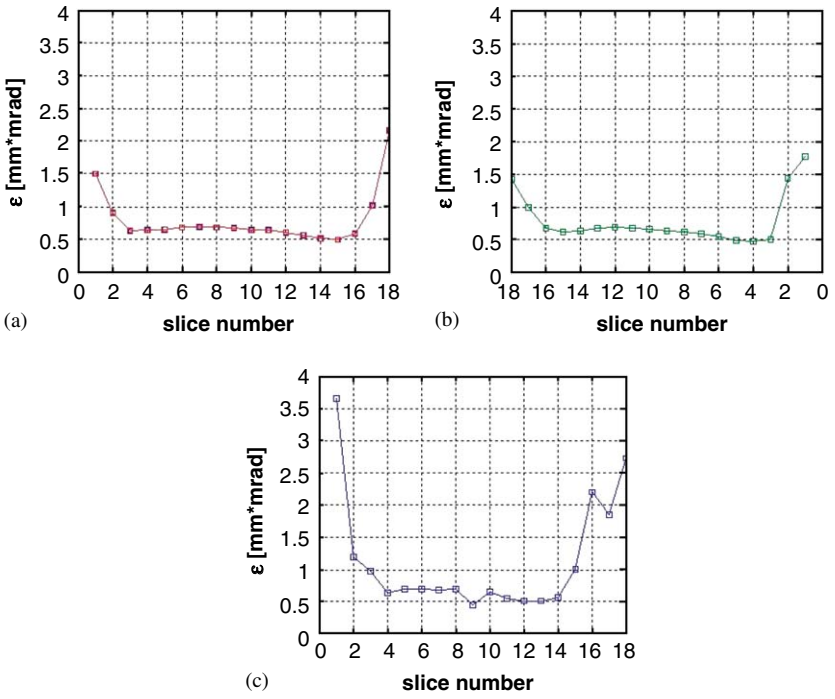

Fig. 11. (a) Horizontal beam slice emittance as a function of slice number; (b) and (c) reconstructed horizontal beam slice emittance by quadrupole scan at the flag F0 and F3, respectively.

where B_x and E_y are the magnetic and electric transverse field components (with the proper phase), L_c is the cavity length, P the dissipated power in the cavity and ω_{RF} the angular frequency.

The dispersion curves of the single cell (obtained by MAFIA) are reported in Fig. 14. The deflecting π mode has the frequency equal to 2.856 GHz, while the nearest monopole and dipole modes are far away from the deflecting one.

Different deflecting structure parameters and related scaling laws[2] are given in Table 3 as a function of the number of cells n. These results have allowed choosing the number of cells for the SPARC deflecting structure. The choice has been done taking into account the following constraints:

(a) the available space in the SPARC transfer line;
(b) the available transverse deflecting voltage for a given input power;
(c) the mode separation with different number of cells to avoid problems of mode overlapping;
(d) the maximum acceptable surface peak electric field to avoid problems related to high field intensities, discharges and so on.

The 5-cell deflecting structure fulfills all of the stated requirements. In fact, it allows operating with a very low

[2]The scaling laws are empirical and have been obtained from the analysis of different simulation results.

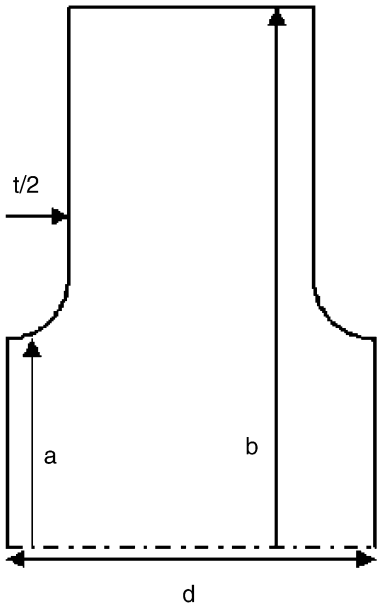

Fig. 12. Single cell of the RF deflector.

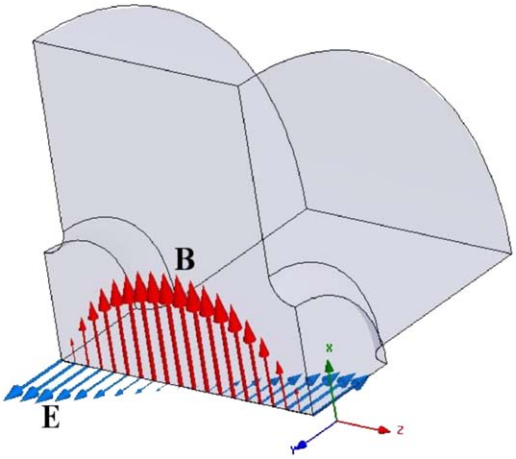

Fig. 13. Field profiles of the deflecting TM_{110}-like mode.

input power $P_{RF} \leqslant 2$ MW obtaining contemporary low peak surface electric field and resolution length of the order of 12 μm. These parameters permit measurement of the longitudinal beam profile with good accuracy, even considering the possibility of longitudinal compression factors up to 20. Moreover the operation at low input power ($P_{RF} \leqslant 2$ MW) allows to simplify the power line design as discussed in Section 6. The complete 2D geometry, without coupler and tuning system, of the 5-cell RF deflector has been studied by using both MAFIA and HFSS and is shown in Fig. 15. The final dimensions, parameters and frequency sensitivities are reported in Table 4. The radius of the cells has been slightly adjusted (especially those of the cells connected to the beam pipe) in order to obtain a *B*-field flatness[3] smaller than 2% as shown in Fig. 16. Concerning this last point it is important to remark that:

1. in multi-cell structures with small irises apertures, since the deflection is given essentially by the magnetic field, the *B*-field flatness implies the uniformity of the deflection given by each cell;
2. in case of a structure with bigger irises, the deflection is given by both the magnetic and the electric fields. Assuming an infinite number of cells, the *B*-field flatness implies, also in this case, the uniformity of the deflection given by each cell;
3. in case of few coupled cells with big irises, nevertheless, the *B*-field flatness does not necessarily imply the uniformity of the deflection given by each cell. In principle, it is possible to find a configuration of the cells radius that makes the transverse deflection uniform from cell to cell [15]. It is, nevertheless, easy to verify that field configurations slightly different from this optimum one (with deflecting force not perfect uniform), give variations of the transverse shunt impedance R_T of a few percent.

From these considerations and also because a uniform *B*-field flatness from cell to cell implies equal dissipation in all the cells (thus maximizing the shunt impedance), the cell radius has been optimized in order to most simply obtain *B*-field flatness.

Concerning the frequency sensitivities with respect to the outer radius of each cell,[4] reported in Table 4, it is possible to conclude that errors in the cell machining of the order of ± 10 μm give resonance frequency errors of the order of ± 100 kHz that can be easily compensated by an appropriate tuning system, as demonstrated in the next section.

4.2. 3D structure design and characterization

Three-dimensional (3D) simulations of the deflecting structure has been performed using HFSS and have been oriented towards:

1. design the input coupler;
2. design the tuning system;
3. design the system to split the frequency of the 90°-tilted polarity with respect to the working one.

The coupler has been inserted in the central cell in order not to excite the 4/5 π mode that has the frequency closest to the π mode, yet has no field in the central cell itself (see Fig. 17). To reduce the coupler window dimensions and, therefore, the perturbation to the deflecting field on the central cell, the smaller dimension (34 mm) of the standard S-band waveguide has been tapered to the dimension of 16 mm. The HFSS-simulated structure is plotted in Fig. 18. We have simulated one-quarter of the deflector with

[3]The *B*-field flatness can be estimated taking the maximum difference of the *B*-field peaks in each cell normalized to the maximum *B*-field value.

[4]The outer radius of each cell is the most critical dimension in terms of sensitivity.

Table 2
Single-cell dimensions, parameters and sensitivities

Dimensions (mm)		Parameters	MAFIA	HFSS	Sensitivities (MAFIA results) (kHz/μm)	
a	20.00	f_{res} (GHz)	2.855925	2.855905	$\partial f_{res}/\partial a$	−19
b	60.01	Q_0	16250	15979	$\partial f_{res}/\partial b$	−43
t	9.50	R_T (MΩ)	0.49	0.49	$\partial f_{res}/\partial t$	1.4
d	52.48	R_T/Q (MΩ)	30.4	30.9	$\partial f_{res}/\partial d$	1.8
		$E_{peak}/\sqrt{P}$ (V/mW$^{-1/2}$)(*)	7.45×10^4	6.92×10^4		

*maximum electric field on the surface.

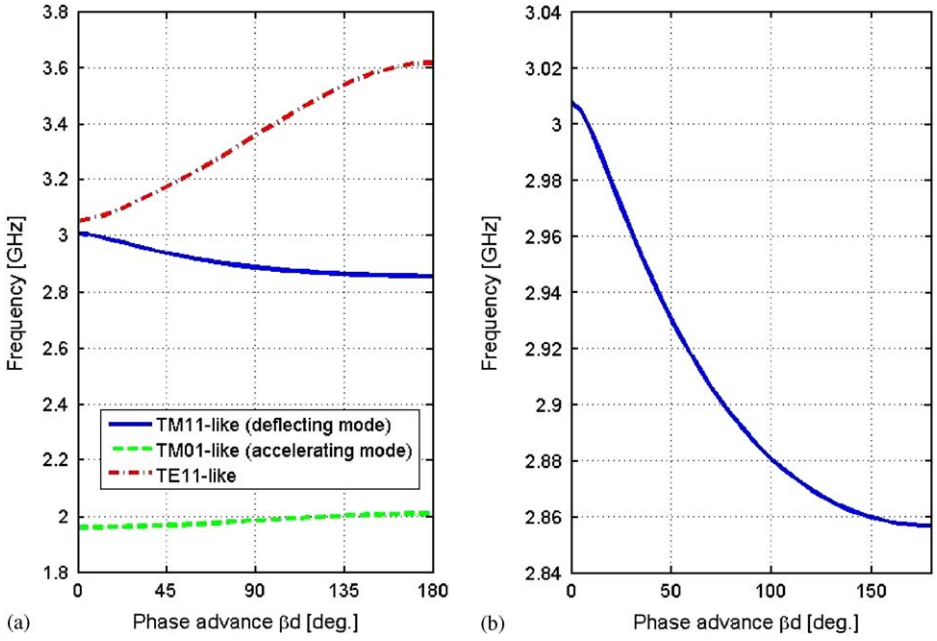

Fig. 14. (a) Single-cell dispersion curves and (b) detail of the deflecting mode dispersion curve (MAFIA results).

Table 3
Deflecting cavity properties as a function of the number of cells and scaling laws

Number of cells	Total length $L \cong 0.0525n$ (m)	Transverse shunt impedance $R_T \cong 0.5n$ (MΩ)	Nearest mode frequency separation $\Delta f \cong 116/n^2$ (MHz)	$E_{peak}/\sqrt{P} \cong 7.4510^4/\sqrt{n}$ (V/mW$^{-1/2}$)
3	0.16	1.5	13	4.31×10^4
5	0.26	2.5	4.6	3.34×10^4
9	0.47	4.5	1.4	2.49×10^4

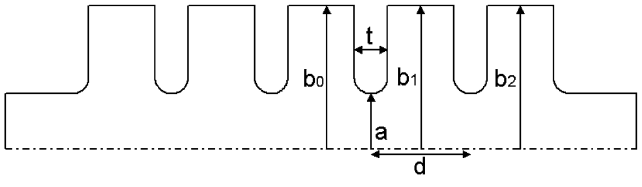

Fig. 15. 2D profile of the 5-cell deflecting structure.

the proper boundary conditions. The dimensions of the coupler window w and of the central cell radius b_0 have been tuned in order to obtain a coupling coefficient $\beta = 1$, a resonant frequency of the whole system equal to 2.856 GHz and to preserve a good B-field flatness. This has been done by following two steps:

1. a single cell with coupler has been simulated, tuning the dimensions of the coupler window and cell radius to obtain a coupling coefficient $\beta = 5$ (five times the coupling coefficient that we would reach with the complete structure) and a cell resonant frequency equal to 2.856 GHz;
2. the complete structure has been simulated starting from the dimensions found in the previous case and adjusting the dimensions of the coupler cell, window and

Table 4
5-cell structure dimensions, parameters and sensitivities

Dimensions (mm)		Parameters	HFSS	MAFIA	Sensitivities (MAFIA) (kHz/μm)	
b_0	60.04	f_{res} (GHz)	2.855961	2.855596	$\partial f_{res}/\partial b_0$	−9.6
b_1	59.93	Q_0	16540	16329	$\partial f_{res}/\partial b_1$	−10.5
b_2	60.72	R_T (MΩ)	2.44	2.40	$\partial f_{res}/\partial b_2$	−8.1
a	20.00	R_T/Q (MΩ)	148	147		
t	9.5	$E_{peak}/\sqrt{P}$	3.33×10^4	3.40×10^4		
d	52.48	(V/[mW$^{-1/2}$])				

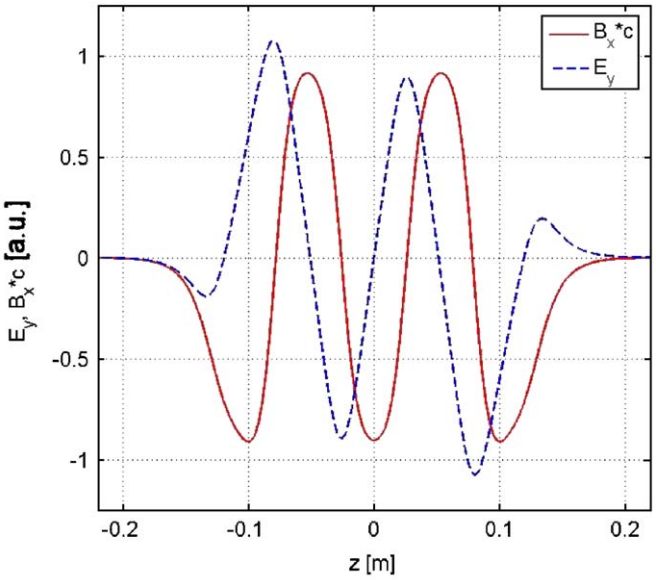

Fig. 16. B and E field of the 5-cell cavity obtained by MAFIA 2D.

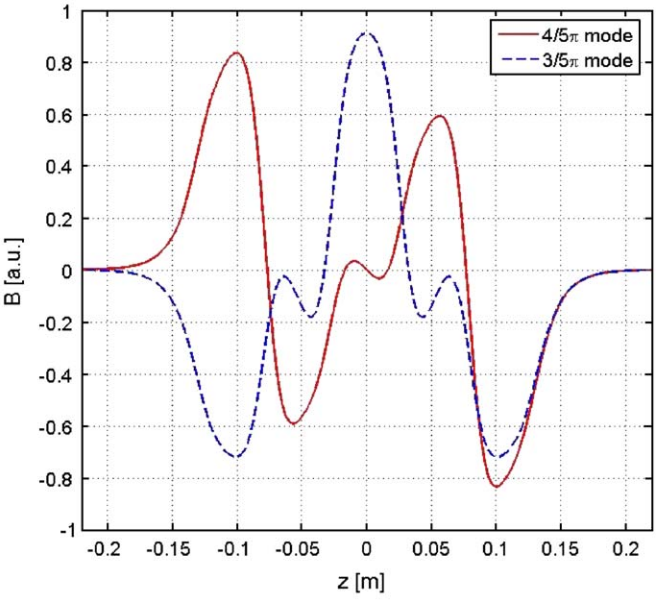

Fig. 17. B field profiles of the $4\pi/5$ and $3\pi/5$ modes.

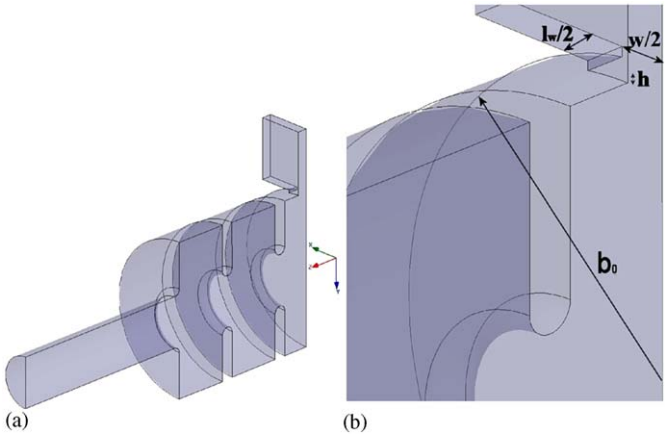

Fig. 18. 3D HFSS simulated structure with coupler.

cell dimensions to obtain $\beta = 1$, $f_{RF} = 2.856\,\text{GHz}$ and B-field flatness.

After this optimization we have obtained the dimensions and the final structure parameters reported in Table 5. The reflection coefficient at the input port is plotted in Fig. 19.

A complete analysis has been performed in order to calculate the frequency separation between the working deflecting mode and the other modes. It is important to distinguish between the four deflecting TM_{110}-like modes with the same polarity of the working mode, and those having polarity rotated by 90°. Concerning the first category, the closest $4\pi/5$ mode at 2.860 GHz is (in principle) not excited by the coupler and it can, therefore, negligibly perturb only the deflecting field. The nearest mode with the same polarity that can be excited by the coupler is the $3\pi/5$ mode (shown in Fig. 17) whose frequency is about +20 MHz away from the working one. To prevent the excitation of the modes with polarity rotated at 90°, two longitudinal rods (of radius $r = 1.5\,\text{mm}$) crossing the cells off-axis have been inserted, as shown in Fig. 20. The resonance frequencies of such modes are shifted far enough from the operating mode frequency (even if, in principle, they are not excited by the central coupler) to be ignorable. The calculated frequency shift for the rotated modes due to the rods is about +50 MHz, while the working mode is practically unperturbed.

Table 5
RF deflector final dimensions and parameters obtained with HFSS

Dimensions [mm]		Parameters	Driven solution	Eigenmode solution
b_0	60.04	f_{res} (GHz)	2.856152	2.856178
b_1	59.93	Q_0	15240	16312
b_2	60.72	R_T (MΩ)	2.24	2.39
a	20.00	R_T/Q (MΩ)	147	147
t	9.5	$E_{peak}/\sqrt{P}$ (V/mW$^{-1/2}$)	3.39×10^4	3.35×10^4
l_w	16.0	β	1	/
w	19.0			
h	1.1			

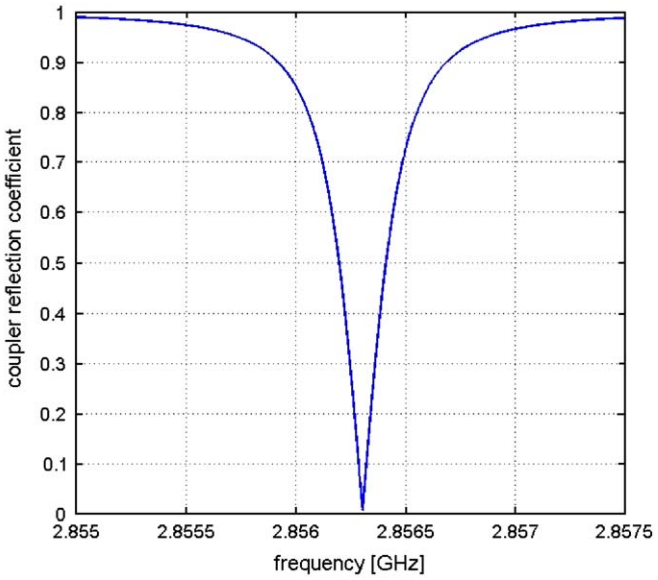

Fig. 19. Reflection coefficient at the input port obtained with HFSS.

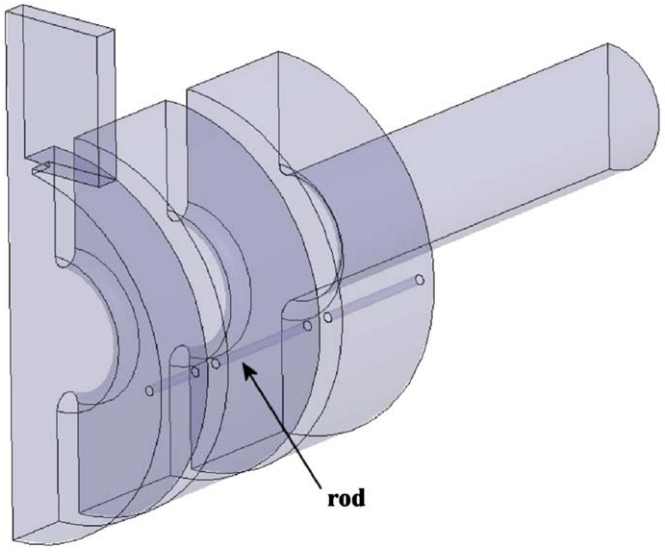

Fig. 20. Longitudinal rods to split the mode frequency of the 90°-rotated polarity modes.

Finally, for the tuning system, we plan to use a cylindrical tuner of $r = 5$ mm that gives a sensitivity of about 500 kHz/mm in the resonant frequency of each cell. The possible machining errors can be therefore compensated by a penetration of the tuners of a few mm.

5. Prototype measurement results

A full scale aluminum prototype has been constructed and is shown in Fig. 21. The cells are joined by six rods. To probe the field in the structure we have also inserted four lateral small antennas coupled with the working mode and with the rotated polarity modes. The details of the tuning system, coupling window and rods are all given in Fig. 21. The prototype has been constructed in order to:

1. measure the resonant frequency and input port coupling coefficient;
2. measure the EM field of the working mode by the bead-pull technique [16];
3. completely characterize the other modes of the RF deflector in term of frequency and EM field.

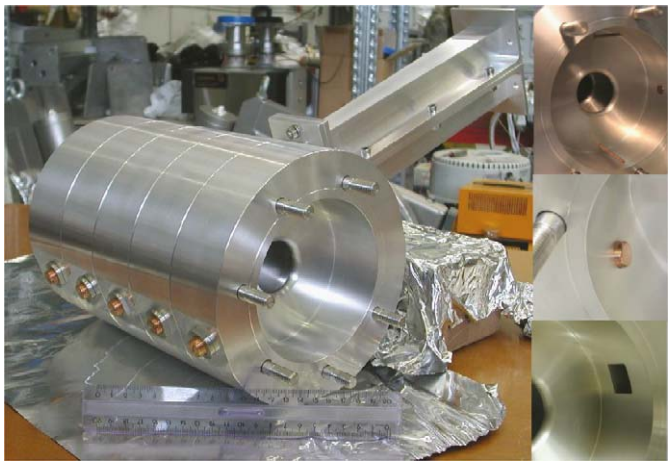

Fig. 21. Deflector aluminum prototype and details of the coupling window, tuning system and rods.

5.1. Resonant frequency and input port coupling measurements

The reflection coefficient at the coupler input port after the tuning procedure is reported in Fig. 22. As expected, it

is possible to excite only three of the five deflecting modes with the input coupler. The measured external quality factor of the working mode is $Q_{EXT} \cong 17000$, in agreement with the simulation results,[5] while the measured unloaded quality factor Q_0 is about 6300 and is lower than what we expected with aluminum ($Q_0 = 14000$) because of the fact that the structure is simply assembled and not welded. Concerning the rotated polarity, in Fig. 23 the transmission coefficients between the two probes coupled with the working mode and that between the two probes coupled with rotated polarity are shown. As expected the rotated polarity has a frequency shift more than 50 MHz.

5.2. Bead-pull measurements results

The measurements of the field in the cavity have been done with the bead-pull technique. The complete measurement setup is shown in Fig. 24. The PC controls both the network analyzer Agilent N5230A (interfaced by a GPIB ethernet device) and the control circuit of the steeping motor through Labview [17]. The nylon wire is kept straight by a 75 g weight. Since the deflection is given by both the magnetic and the electric field, both components have to be measured for a correct characterization of the device. Two types of perturbing objects have been used to measure the B–E field components: a small dielectric (teflon) cylinder (Fig. 25(a)) and a small metallic sphere (Fig. 25(b)). With the first object we have measured the E field component only while, with the second one, both the B and E field components. The used formulas were:

$$\text{dielectric bead}: \quad \frac{\Delta f}{f_0} = \varepsilon_0 \frac{1-\varepsilon_r}{2+\varepsilon_r}\left(k_{Edz}\frac{|E_z|^2}{W} + k_{EdT}\frac{|E_T|^2}{W}\right)$$

$$\text{metallic bead}: \quad \frac{\Delta f}{f_0} = -\varepsilon_0\left(k_{Emz}\frac{|E_z|^2}{W} + k_{EmT}\frac{|E_T|^2}{W}\right) + \mu_0\left(k_{Bmz}\frac{|B_z|^2}{W} + k_{BmT}\frac{|B_T|^2}{W}\right) \tag{7}$$

Here Δf is the resonant frequency variation[6] with respect to the unperturbed frequency f_0, W the total energy stored in the cavity and k_E, and k_B are the form factors associated with the E or B field, with the subscripts d and m indicating the dielectric and metallic objects, respectively, and z or T indicating the longitudinal or the transverse components of the field. On axis, we have for deflecting modes $B_z = 0$ and $E_z = 0$.

[5]Especially if we consider that, in the aluminum prototype there are strong losses and Q_0 is strongly perturbed.

[6]Instead of the Δ frequency one can measure the Δ phase ($\Delta\phi$) of the transmission coefficient between two ports coupled with the field in the cavity since it is related to the frequency variation through the formula: $\tan\Delta\phi = (\Delta f/f_0)2Q_L$ where Q_L is the loaded quality factor of the resonance [18].

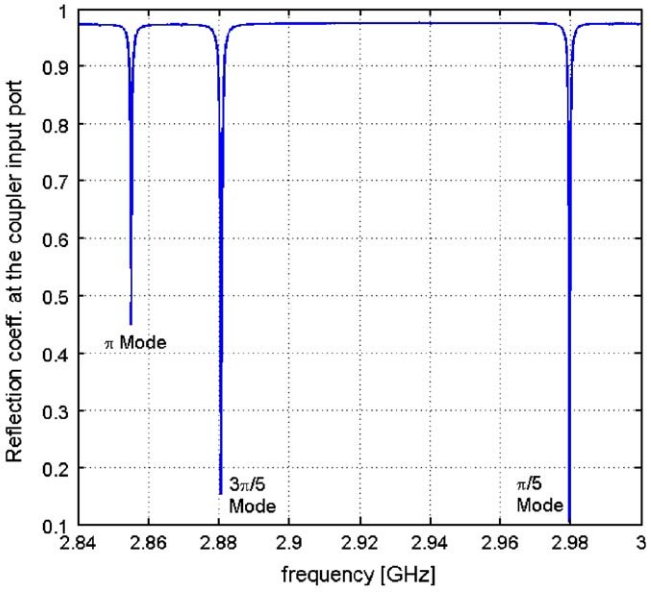

Fig. 22. Measured reflection coefficient at the input coupler port.

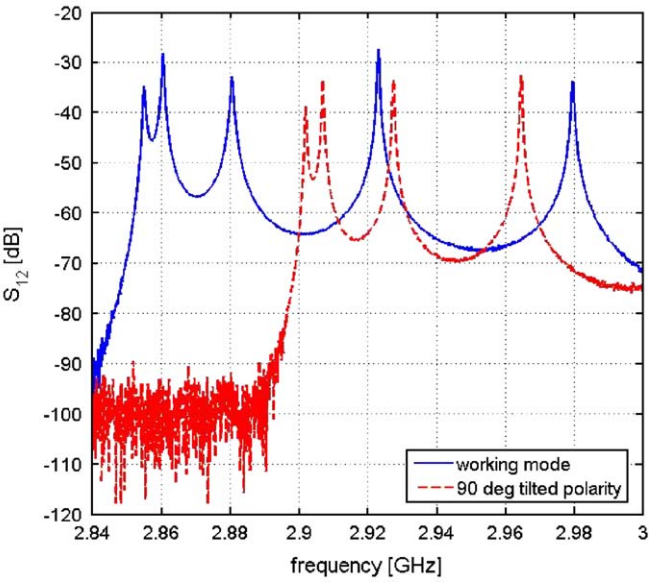

Fig. 23. Transmission coefficient between the two antenna coupled with the working mode and between the two antenna coupled with the 90°-rotated polarity.

In order to extrapolate the transverse magnetic field components one can proceed by following these two different ways:

1. if one is interested in the measurements of the magnetic field profile and not in its absolute value, one can simply scale the result of the first measurement in order to subtract the contribution of the electric field from the second one. Looking, in fact, at the field profile components reported in Fig. 16 the two central peaks of the electric field correspond to zero crossing of the magnetic field. Therefore it is straightforward to

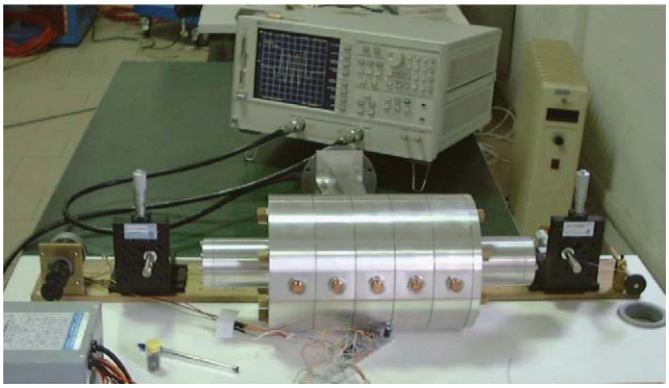

Fig. 24. Bead-pull measurement setup.

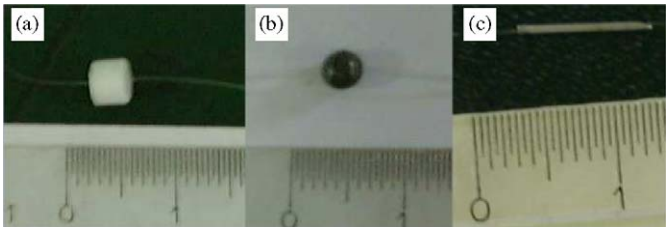

Fig. 25. Perturbing objects employed: (a) dielectric cylinder; (b) metallic sphere and (c) metallic needle.

subtract the contribution of the electric field from the second measurement, just scaling the first measurement results by making equal the peaks of the electric field. These type of measurements can be useful if one is interested, for example, in B field flatness tuning only;

2. if one is interested in the measurement of the absolute value of the B field one has to calibrate the perturbing objects by doing measurements on different modes on a simple geometry (e.g., pillbox cavity) and calculating the coefficients through Eqs. (7).

To calibrate the perturbing objects we have used the pillbox cavity shown in Fig. 26. The resonant modes used were the TM_{110} mode (having no E field component on axis) to calculate the $k_{B\mathrm{m}}$ factor and the TE_{111} mode (having no B field component on the center of the cavity) to calculate the $k_{E\mathrm{d}}$ and $k_{E\mathrm{m}}$ factors.

It is possible, also, to calculate the total deflection given to the particles by integrating the longitudinal electric field component off axis and by using the Panofky–Wenzel theorem [19]. To do this it is possible to use a small metallic needle (Fig. 25(c)), with a previously calibrated form factor k_{Emz}. To calibrate the needle we have used the TM_{010} mode of the pillbox cavity.

The final measurement results are summarized in Figs. 27–30. The results of the measurements using the metallic sphere and the dielectric cylinder are reported in Fig. 27, where the average curves calculated over 30 measurements are plotted; the B field profile is sketched as well (green curve) and it has been calculated by the subtraction of the previous measurements as discussed above. The maximum standard

Fig. 26. Pillbox cavity used for calibration of perturbing objects.

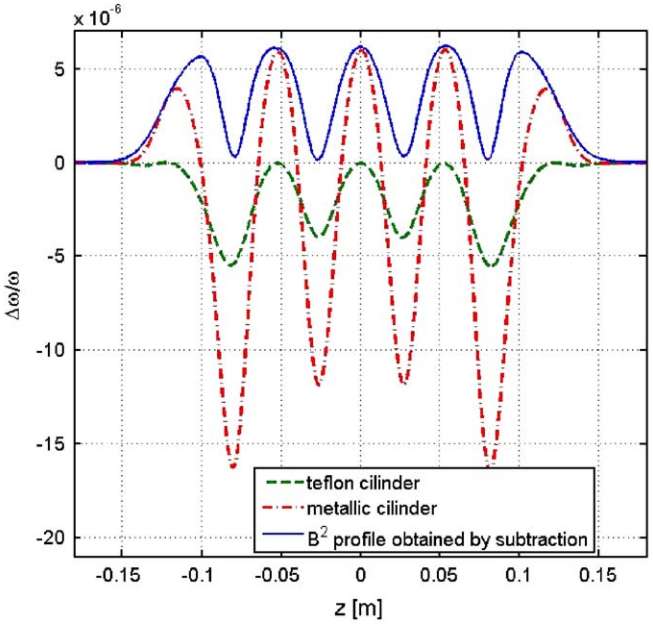

Fig. 27. Results of the measurements using the metallic and the dielectric cylinder: average curves calculated over 30 measurements and B field profile calculated by subtraction.

deviation of measurements were about 1×10^{-7} in case of dielectric cylinder and 7×10^{-7} in case of metallic cylinder.[7]

In Fig. 28 we plot the B and E field components obtained by calibrating the measurements with the form factor found with the pillbox. In the same figure are plotted the simulation results obtained by MAFIA.

[7]We define the average curves and the maximum standard deviation as follows:

(a) we have plotted the 30 measurements with the same longitudinal coordinate;
(b) for each longitudinal coordinate we have calculated an average value and a standard deviation;
(c) we have defined the average curve as the ensemble of the average values and the maximum standard deviation as the maximum of the standard deviations previously calculated.

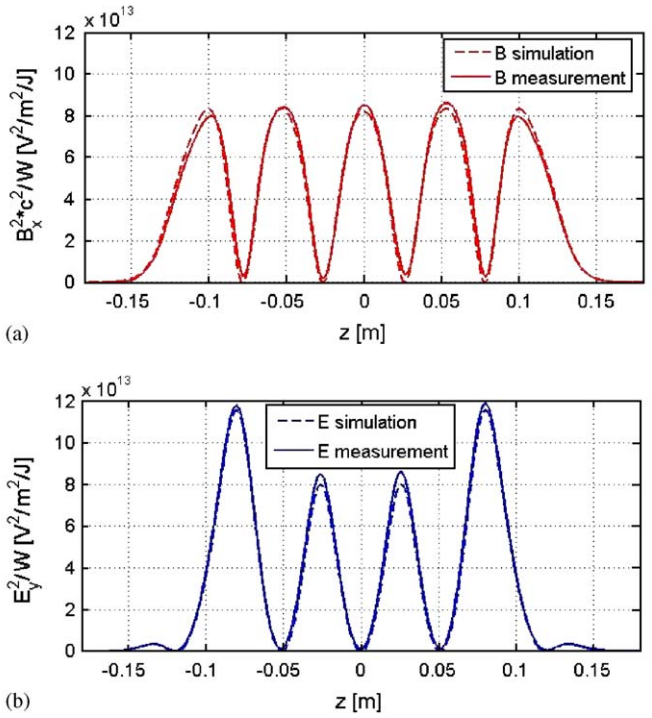

Fig. 28. B and E field components (plots (a) and (b), respectively) obtained by calibrating the measurements with the form factor and comparison with simulation results obtained by MAFIA.

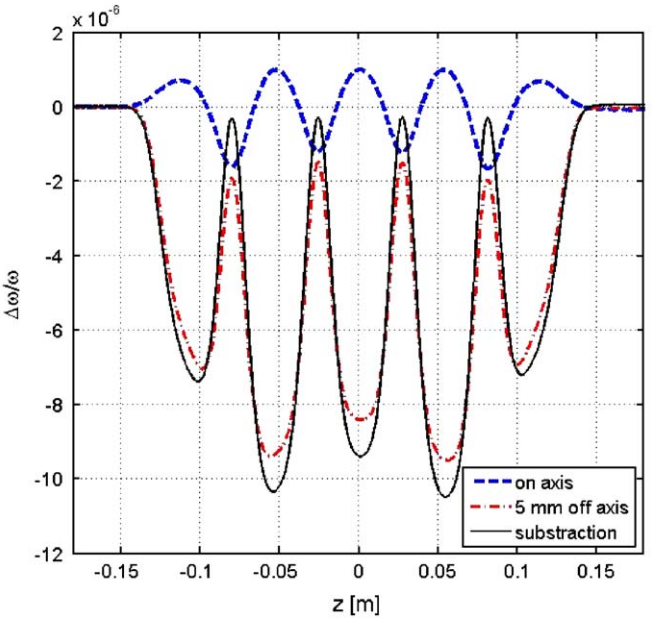

Fig. 29. Measurement results obtained with a metallic needle on axis and 5 mm off axis. The longitudinal electric field component off axis has been obtained by simply subtracting the two measurements.

Finally, in Fig. 29, the measurement results obtained with a metallic needle on axis and 5 mm off axis[8] are given. The off-axis longitudinal electric field component has been obtained by simply subtracting the two measurements since the transverse E and B field components (affecting the measurements of the longitudinal electric field off axis) do not vary, to the first order, with the transverse coordinate. In Fig. 30 the longitudinal E field component obtained by calibrating the measurements with the form factor found with the pillbox is shown. In the same figure there are plotted the simulation results obtained by MAFIA.

[8]In the figure there are plotted the average curves calculated over 30 measurements. The standard deviation of the measurements is 3×10^{-7} in the case of the off-axis measurement and 1×10^{-7} in the on-axis case.

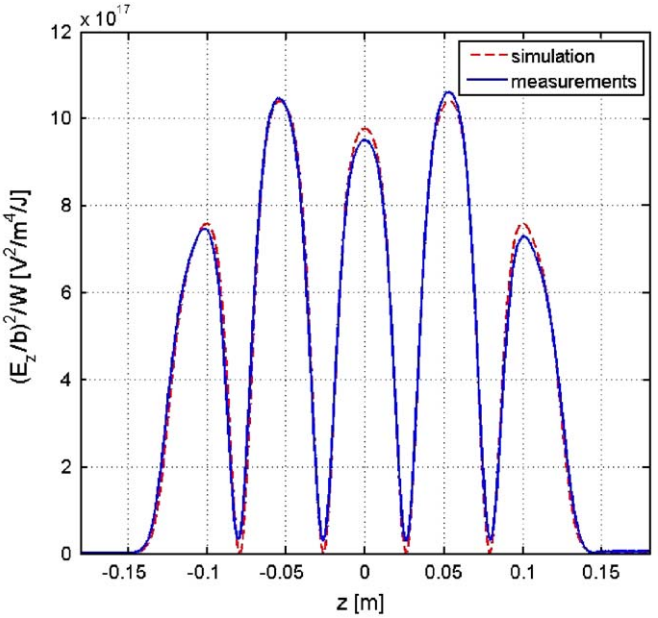

Fig. 30. Longitudinal E field component normalized to the bead displacement from the axis b and comparison with simulation results obtained by MAFIA.

6. RF deflector power feeding system

The 2 MW input power needed to feed the structure can be split out from the first klystron waveguide feed with a 10 dB directional coupler, as illustrated in Fig. 31. The circulator and the directional coupler assure that the reflected power from the deflector does not interact with the power feeding the RF gun. Moreover the high-power switch is included to allow the deflecting field to be completely turned off.

Because of the relatively low power needed for the structure it is possible to simply employ an air-filled waveguide system, thus reducing the cost of the entire power feed system.

7. Conclusion

In the first section of this paper we have discussed our intended technique to completely characterize the longitudinal and transverse phase space at SPARC.

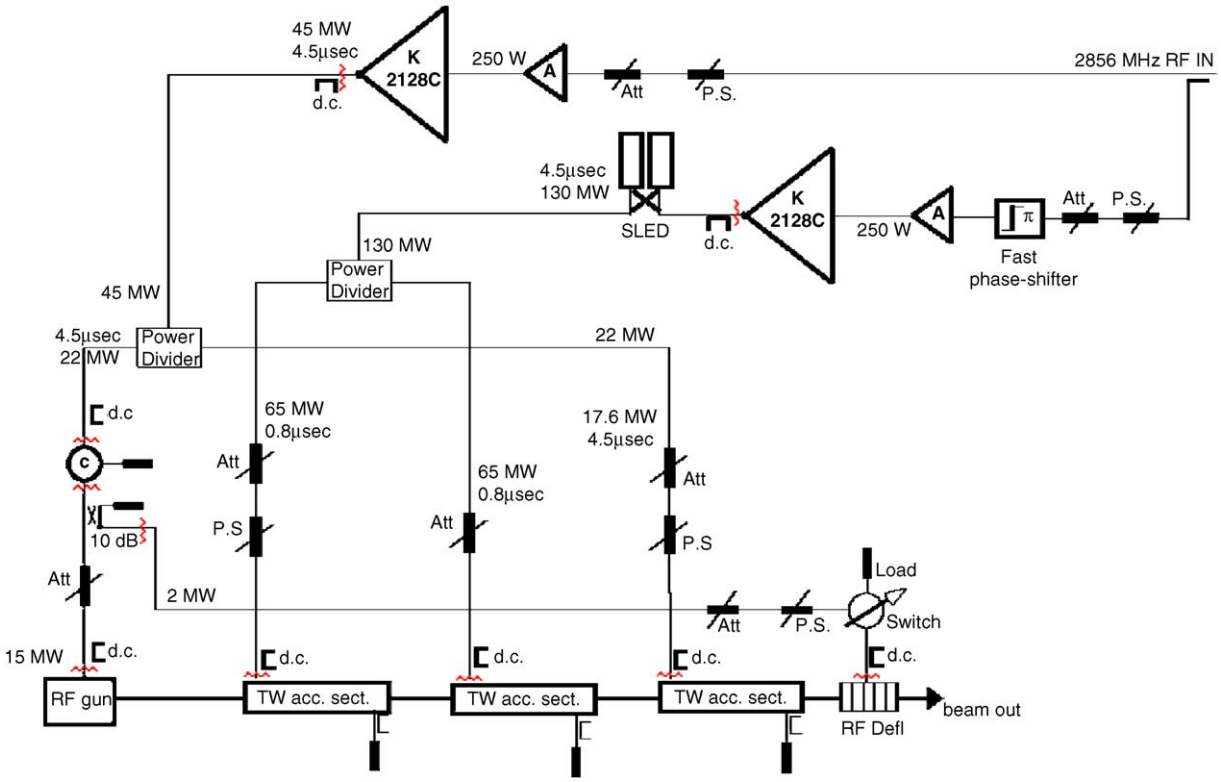

Fig. 31. Sketch of the RF deflector power feed system.

The methods are based on the use of an RF deflector that allows measuring the temporal profiles of the beam, as well as the complete longitudinal phase space by adding a dispersive system. Using the quadrupole scan technique the horizontal beam slice emittances as a function of longitudinal position in the beam can also be measured. Simulations made by the ELEGANT code have shown the feasibility of this diagnostic system.

In second part of the paper we have illustrated the RF deflector design procedure made by the use of the e.m. codes MAFIA and HFSS. The RF deflector proposed is a 5-cell SW structure working on the π mode at 2.856 GHz and fed by a central coupler with $\beta = 1$. Since the transverse shunt impedance is $\approx 2.5\,\mathrm{M\Omega}$ and the maximum input power is 2 MW, it is possible to obtain a resolution length of the order of 12 μm. Two small longitudinal rods have been inserted to shift the resonant frequency of the 90°-rotated polarity modes with respect to the working mode. In the last part of the paper we have discussed the measurement results made on an aluminum prototype of the deflector. By the bead-pull technique we have measured the deflecting field on axis. A tuning procedure has been implemented in order to reach a field flatness of the order of a few percents. External quality factor measurements have also been done, showing good agreement with expectations.

Acknowledgment

This work has been partially supported by the EU Commission in the sixth framework program, Contract no. 011935 EUROFEL-DS1.

References

[1] Preliminary technical design report for the SPARC advanced photo-injector, ⟨www.lnf.infn.it⟩, 2004.
[2] G.A. Loew, O.H. Altenmueller, Design and applications of RF deflecting structures at SLAC, PUB-135, August 1965.
[3] P. Emma, et al., A Transverse RF deflecting structure for bunch length and phase space diagnostics, LCLS-TN-00-12, 2000.
[4] D.H. Dowell, et al., Slice emittance measurements at the SLAC Gun Test Facility, SLAC-PUB-9540, September 2002.
[5] J.F. Schmerge, et al., Nucl. Instr. and Meth. A 483 (2002) 301.
[6] X. Qiu, et al., Phys. Rev. Lett. 76 (20) (1996) 3723.
[7] D.T. Palmer, The next generation photoinjector, Ph.D. Thesis, Stanford University, 1998.
[8] J. Billen, PARMELA, LA-UR-96-1835, 1996.
[9] M. Borland, Elegant, a flexible SDDS-compliant code for accelerator simulation, LS-287, Argonne National Laboratories, April 2000.
[10] D. Alesini, C. Vaccarezza, Longitudinal and transverse phase space characterization at SPARC, SPARC Note, 2003.
[11] P. Bernard, H. Lengeler, On the design of disc-loaded waveguides for RF separators, CERN 68-30, Geneva, 1968.
[12] R.E. Collin, Foundations for Microwave Engineering, McGraw-Hill, New York, 1992, pp. 504–508.
[13] ⟨www.cst.de⟩.
[14] ⟨www.ansoft.com⟩.

[15] L. Ficcadenti, Caratterizzazione e ottimizzazione di una cavita deflettente a RF, Degree Thesis, University of Rome, La Sapienza, 2004.
[16] L.C. Maier Jr., J.C. Slater, Field strenght measurement in resonant cavities, J. Appl. Phys. 23 (1) (1951).
[17] National Instruments LabVIEW, 〈www.ni.com\labview〉.
[18] F. Casper, G. Dome, Precise perturbation measurements of resonator cavities and higher order mode identification, CERN SPS/85-46 (ARF), November 1985.
[19] G. Dome, Basic RF theory, waveguides and cavities, RF engineering for particle accelerators, CAS-Cern Accelerator School, CERN 92-03, Geneva, 1992.